Local tuning of WS$_2$ photoluminescence using polymeric micro-actuators in a monolithic van der Waals heterostructure

Francesco Colangelo ID, Andrea Morandi, Stiven Forti, Filippo Fabbri, Camilla Coletti ID, Flavia Viola Di Girolamo, Alberto Di Lieto, Mauro Tonelli ID, Alessandro Tredicucci ID, Alessandro Pitanti ID, and Stefano Roddaro

View Online   Export Citation   CrossMark

ARTICLES YOU MAY BE INTERESTED IN

Local tuning of WS₂ photoluminescence using polymeric micro-actuators in a monolithic van der Waals heterostructure

Francesco Colangelo,[1,a),b)] Andrea Morandi,[1,2,b),c)] Stiven Forti,[3] Filippo Fabbri,[1,3,4] Camilla Coletti,[3,4] Flavia Viola Di Girolamo,[2,d)] Alberto Di Lieto,[2] Mauro Tonelli,[2] Alessandro Tredicucci,[1,2,5] Alessandro Pitanti,[1,a)] and Stefano Roddaro[1,2]

AFFILIATIONS

[1]NEST, Scuola Normale Superiore and Istituto Nanoscienze-CNR, Piazza S an Silvestro 12, I-56127 Pisa, Italy
[2]Department of Physics "E. Fermi," University of Pisa, Largo Bruno Pontecorvo 3, I-56127 Pisa, Italy
[3]Center for Nanotechnology Innovation @NEST, Istituto Italiano di Tecnologia, Piazza San Silvestro 12, I-56127 Pisa, Italy
[4]Graphene Labs, Istituto Italiano di Tecnologia, Via Morego 30, I-16163 Genova, Italy
[5]Fondazione Bruno Kessler (FBK), Via Sommarive 18, 38123 Povo, Trento, Italy

[a)]Authors to whom correspondence should be addressed: francesco.colangelo@sns.it and alessandro.pitanti@sns.it
[b)]Contributions: F. Colangelo and A. Morandi contributed equally to this work.
[c)]Present address: Optical Nanomaterial Group, Institute for Quantum Electronics, Department of Physics, ETH Zürich, Auguste-Piccard-Hof 1, 8093 Zürich, Switzerland.
[d)]Present address: Istituto Nazionale di Fisica Nucleare, L.go Bruno Pontecorvo 3, 56127 Pisa, Italy.

ABSTRACT

The control of the local strain profile in 2D materials offers an invaluable tool for tailoring the electronic and photonic properties of solid-state devices. In this paper, we demonstrate a local engineering of the exciton photoluminescence (PL) energy of monolayer tungsten disulfide (WS₂) by means of strain. We apply a local uniaxial stress to WS₂ by exploiting electron-beam patterned and actuated polymeric micrometric artificial muscles (MAMs), which we implement onto monolithic synthetic WS₂/graphene heterostructures. We show that MAMs are able to induce an in-plane stress to the top WS₂ layer of the van der Waals heterostructure and that the latter can slide on the graphene underneath with negligible friction. As a proof of concept for the local strain-induced PL shift experiments, we exploit a two-MAM configuration in order to apply uniaxial tensile stress on well-defined micrometric regions of WS₂. Remarkably, our architecture does not require the adoption of fragile suspended microstructures. We observe a spatial modulation of the excitonic PL energy of the WS₂ monolayers under stress, which agrees with the expected strain profile and attains a maximum redshift of about 40 meV at the maximum strain intensity point. After the actuation, a time-dependent PL blueshift is observed in agreement with the viscoelastic properties of the polymeric MAMs. Our approach enables inducing local and arbitrary deformation profiles and circumvents some key limitations and technical challenges of alternative strain engineering methods requiring the 2D material transfer and production of suspended membranes.

Published under license by AIP Publishing. https://doi.org/10.1063/1.5122262

Among the wide number of existing two-dimensional (2D) materials,[1,2] transition metal dichalcogenides (TMDs)[3,4] have gained preferential attention due to their gapped electronic structure for their possibility of efficiently emitting light, even at room temperature,[5] and for their wide possible applications when stacked in van der Waals heterostructures.[6–8] Monolayer tungsten disulfide[9] (WS₂) is one of the TDMs and shows a strong photoluminescence (PL) around 2 eV.[10] The PL of WS₂ mostly originates from the recombination of neutral excitons,[11] and its energy is expected to be a function of the local strain[12–17] of the layer. Enabling the local control of strain in WS₂, and in general in TMDs, can give access to the observation of many interesting physical phenomena such as exciton funneling,[18–20] optical anisotropy and local bandgap modulation,[21,22] and pseudomagnetic fields;[17,23,24] all these phenomena can be explored in a wide range of strain thanks to the remarkably good mechanical properties of monolayer WS₂.[25] Common methods to strain 2D materials exploit the

substrate deformation.[12,14,15,26–31] These methods offer in principle a good degree of control on the strain magnitude, but they do not allow a local design of the strain profile. On the other hand, alternative approaches such as the direct growth or the transfer of TMDs onto nonflat substrates emerged as promising routes to achieve strongly localized strain puddles.[19,21,32–34] However, these methods lack control on the induced strain. The use of suspended 2D material structures has been demonstrated to be an effective way to design nonhomogeneous, and even anisotropic strain profiles on micrometric scales, either by using a pressure load[35–37] or microelectro mechanical strain platforms.[38–40] But additional difficulties arise when working with suspended 2D layers due to the fragility of devices and the formation of random strain puddles during the nanofabrication.[41] Similar limitations hold also for nanoindented suspended membranes that, while they can be an intriguing approach to study the effect of strain at the nanoscale,[18,42,43] at present they have been solely used to characterize the mechanical properties of 2D materials.[25,41,44] As a consequence, inhomogeneous and anisotropic strain profiles have been poorly explored in most of the 2D materials, and WS_2 monolayers have been strained only by employing bendable/stretchable substrates[12,14,15,31] or substrate thermal expansion,[16] thus only attempting homogeneous strain configurations.

Nevertheless, an appealing alternative strain engineering technique has been recently developed by some of us, and it has demonstrated to be suitable to generate a wide range of controlled, spatially inhomogeneous, and anisotropic strain fields in suspended graphene,[45] but in principle, it can be applied to other 2D materials as well. Indeed, the technique exploits patternable polymeric micrometric actuators or micrometric artificial muscles (MAMs), made of poly-methyl-methacrylate (PMMA), which contract when irradiated by a sufficiently high dose of electrons. Here, we combine MAMs with the low-friction properties of WS_2 grown on top of graphene on silicon carbide (SiC),[46,47] and thus, we realize localized and anisotropic in-plane strain fields in monolayer WS_2 in a supported configuration. We demonstrate a strain-engineered spatially modulated redshift of the WS_2 PL energy, with a maximum energy shift of about 40 meV. Moreover, we show that the preparation of an initial strain state is followed by a PL shift as a function of time due to the viscoelasticity property of the employed MAMs. This relaxation allows us to unequivocally identifying strain as the source of the PL shift and gives access to intermediated states at lower strain in a continuous way. The described approach is based on a monolithic synthetic van der Waals heterostructures; it is scalable[48] and does not require any transfer procedure.[49] Moreover, it allows defining multiple devices with different and custom strain profiles on the very same sample, and it is expected to work with most of the 2D materials.

The fabrication of the sample starts with the growth of graphene on 6H-SiC(0001) chips by thermal decomposition (see the supplementary material). This well-established procedure can be used to obtain very large areas (centimeter-size regions) of single and multilayer graphene. In our case, we grow two graphene layers, i.e., a bilayer of graphene (BLG) on SiC to improve the overall flatness of the sample. In a final growth step, WS_2 is grown on top of the BLG by chemical vapor deposition (CVD), starting from S and WO_3 powders as solid precursors (see the supplementary material for further details). From the resulting shape of the CVD grown material, it can be assessed that the WS_2 layer consists of a multigrain or polycrystalline film of WS_2,
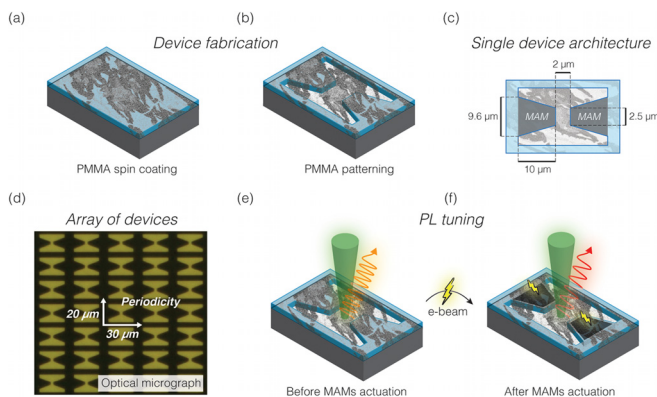
which covers a large portion of the BLG surface (about 50%) and mostly contains regions with one or two monolayers, as visible in the representative atomic force microscopy (AFM) map reported in the supplementary material. Line-profiles of AFM topographic data have been used to identify the different materials from their relative heights. Figure 1(a) shows that the different materials can also be identified by considering contrast levels in scanning electron microscopy (SEM) images by setting the e-beam energy at 2 keV. The material identification is obtained from a cross correlation with PL and AFM maps acquired in the same positions (see the supplementary material). SEM images show that the largest contrast steps are due to the WS_2 layers, as indicated in the figure. Weaker contrast steps are also visible in correspondence of BLG/SiC terraces. The PL of the sample is studied by employing an "inVia Renishaw" system working at a low power of 0.5 mW and collecting the signal with a $100\times$ objective with 0.85 NA. As-grown WS_2 shows a strong room-temperature PL signal when excited with 532 nm laser light. We fitted the light emission of WS_2 with a single Voigt line shape [see Fig. 1(b)], which takes into account inhomogeneous broadening coming from atomic defects, grain boundaries, and the finite laser spot size ($\sim$500 nm). The spatial PL distribution was studied by performing a set of micro-PL maps in different positions of the sample. We characterize the PL signal by fitting the spectrum of each point in the maps, and we observe an average small spatial PL inhomogeneity, mainly due to the partial coverage of monolayers WS_2 and the presence of nanometric adlayers islands, which are expected to affect the emitted light properties.[10,50] The $10.5 \mu m \times 10.5 \mu m$ spatial map of the PL peak position of Fig. 1(c) is representative of the PL properties of our van der Waals heterostacks: no relevant emission can be observed in regions where only graphene is present (black pixels); the remaining regions show an emission peak
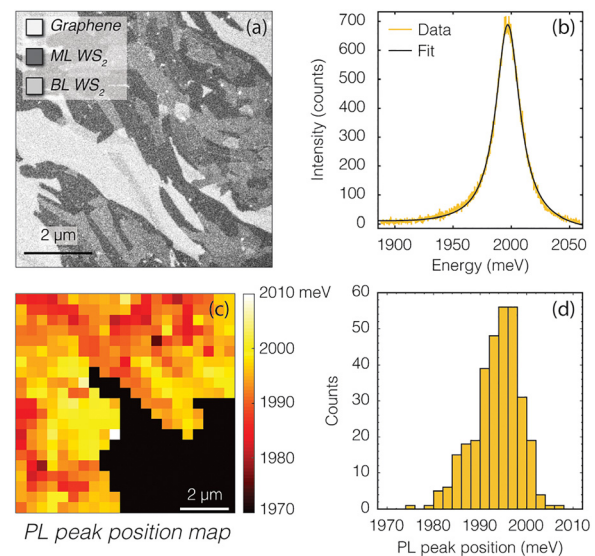
FIG. 1. Characterization of the as-grown sample. (a) The presence of WS_2 layers can be identified by scanning electron microscopy: graphene (bright), monolayer WS_2 (ML, dark gray), and bilayer WS_2 (BL, light gray). (b) Typical PL spectrum obtained on the monolayer (ML) WS_2. (c) Characteristic spatial distribution of the PL peak position. No PL signal is observed in the black pixels, consistently with the absence of WS_2 layers. (d) Histogram of the entries of panel (c); the PL energy range goes from 1980 to 2000 meV.

of variable intensities and centered in the energy range going from 1980 to 2000 meV, as clear from the corresponding histogram in Fig. 1(d). In summary, our sample consists of continuous BLG with on top micrometric areas of monolayer WS_2, which form the van der Waals heterostructures and which show good PL properties. Although the WS_2 regions are randomly distributed and partially cover the sample surface, they can be quickly individuated using SEM imaging and exploited for strain-engineering experiments.

The two-MAM device architecture employed for the strain engineering experiments is sketched in Fig. 2. After the preliminary characterization, the sample is spin-coated with PMMA (AR-P 679.04) for 60 s at 4000 rpm and then soft-baked for 15 min at 90 °C to evaporate the resist solvent. As a result, a uniform 110 nm thick layer of PMMA covers the whole sample surface [Fig. 2(a)]. Then, we use standard e-beam lithography to pattern into the PMMA layer, a set of "access windows" revealing portions of the WS_2 top surface, and alignment markers, see Fig. 2(b). Each access window identifies a single device. The two horizontal trapezoidal regions of PMMA implement the two opposite pulling MAMs that will contract when exposed to a high dose of electrons. It is worth noting that such a design ensures that one of the two ends of each MAM is embedded—and thus anchored—to the external PMMA frame, while the opposite MAM tips are free from the mechanical load of PMMA. In this way, even if the two MAMs are supported by a superlubric layer, they can still apply a tensile stress to the material in between them. In addition, the PMMA removal allows SEM and AFM imaging of the sample on the strain-engineered regions. The nominal distance between the tips of the two MAMs is 2 μm and corresponds to the typical size of the monolayer WS_2 domains of our sample. A detailed scheme depicting the architecture of devices is reported in Fig. 2(c). It is worth underlining that this approach is easily scalable, and many devices can be prepared in a single lithographic step, as shown in the optical micrograph of Fig. 2(d), which shows a portion of the batch of the 600 fabricated devices. A set of 20 devices was used for WS_2 pulling experiments, while many others were exploited for explorative tests and calibrations;

a quick device screening is possible thanks to the compatibility of the technique with *in situ* SEM imaging and allows selecting devices with a continuous layer of WS_2 between the pair of MAMs for strain engineering experiments. The actuation of the MAMs is obtained by exposing both the trapezoidal PMMA regions with equal doses and using an e-beam energy of 2 kV. By contraction, the MAMs are expected to induce a specific strain pattern in the WS_2 layer and therefore to write a specific spatial pattern of the WS_2 PL energy. Indeed, as mentioned before, the exciton PL depends on the local strain. In particular, the PL energy is expected to be proportional to the volumetric component of the strain[12,14–16] (i.e., to the trace of the tensor strain) and mainly due to a change of the material bandgap.[14,17,24] Since the total exposure dose determines the final PMMA shrinkage magnitude, the pulling stress of MAMs and, as a consequence, the magnitude of the induced PL shift can be tuned. In order to have differential measurements of the device properties, SEM, AFM, and PL maps were measured before and after the MAM actuation as sketched in Figs. 2(e)–2(f).

It is worth stressing that the discussed experimental method crucially depends on the ability of WS_2 to slide on top of the graphene layer. Although there are experimental evidence that submicrometric single crystals of WS_2 can slide on top of graphene with negligible friction,[46,47] it is not clear if such a superlubric property holds also for micrometric portions of multigrain WS_2 layers. In order to shed light on the tribological properties of our WS_2/BLG heterostructure interface, we tested devices showing a discontinuous WS_2 layer between the two MAMs, and we pulled and dragged the WS_2 layer for hundreds of nanometers on the BLG underneath. This is possible by exploiting the high shrinkage magnitude (>5%) of MAMs when irradiated with doses of hundreds of mC/cm^2. The results of our sliding tests (see the supplementary material) allow us to conclude that both the static friction and dynamic friction do not play any significant role in our experiments.

The PL properties of WS_2 under stress are investigated by performing a set of micro-PL line scans across the gap between MAMs connected with a continuous layer of WS_2. We used a low pump power of 0.5 mW and an integration time of 1 s, aiming to obtain a good signal-to-noise ratio while minimizing the local heating effect, which is known to influence the viscoelastic relaxation of MAMs.[45] In addition, these experimental conditions allow reducing the total acquisition time for a single PL map on time scales much shorter than the typical relaxation time of MAMs. The step size of the line scans is 500 nm, which approximately corresponds to the laser spot size. A lag time typically ranging from 10 to 15 min exists between actuation and the start of PL measurements. Figure 3 shows the results of a strain engineering experiment performed on one of the devices. A comparison of PL spectra collected on the central region of the device before and after the MAMs exposure is reported in Fig. 3(a). Using an actuation dose of 15 mC/cm^2, we observe a redshift of about 40 meV ($\sim$12 nm in wavelength) of the WS_2 light emission spectrum. Moving away from the central region of the device, the redshift decreases and its spatial modulation is depicted in Fig. 3(b) where a color map of the PL shift overlays the SEM micrograph of the device. The plotted PL shift values are obtained by subtracting pixel-by-pixel the PL energy before and after the actuation. The PL redshift pattern in between the two MAMs can be understood as a consequence of the inhomogeneous MAM-induced strain profile. Indeed, based on our numerical
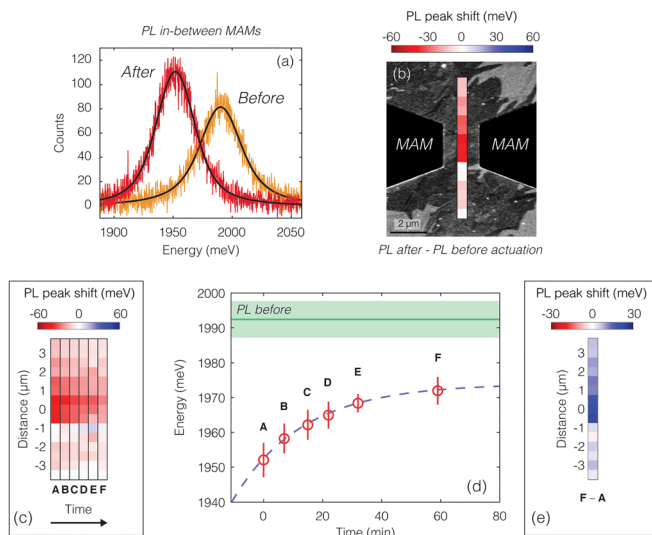

FIG. 2. Device fabrication steps: (a) the as-grown sample is spin-coated in PMMA; (b) selected regions are revealed by e-beam lithography, and alignment markers are defined. (c) Single device architecture details. The two trapezoidal PMMA regions in gray are the one used as MAMs. (d) Optical micrograph of a portion of defied devices. In black is shown the remaining PMMA. After fabrication, the initial PL emission spectrum (e) is compared with the one obtained (f) after the actuation of the MAMs.

FIG. 3. (a) Comparison of two PL spectra acquired at the center of one of the studied devices before and after the MAM actuation. Black lines are best Voigt fits and indicate a PL redshift of about 40 meV. (b) SEM micrograph of the device with a color plot of the PL shift profile in overlay. The reference PL peak position corresponds to the one before the MAM actuation. (c) Consecutive PL shift profiles acquired at different times. (d) Time evolution of the PL peak position (red circles) as the center of the device. The green line indicates the PL energy before the MAM actuation, while the blue dashed line is an exponential best fit. (e) PL shift between the first measurement after the MAM actuation (scan "A") and the last one (scan "F").

simulations (see the supplementary material) and on what already observed in suspended graphene,[45] the strain pattern is expected to be anisotropic, tensile, and strongly localized in between the two MAMs. We note also that the PL shift profile does not exactly match the mirror symmetry of the device architecture, but the discrepancy can be understood based on the nontrivial and asymmetric shape of the studied WS$_2$ flake. It is worth mentioning that during strain-engineering experiments, *in situ* monitoring of devices revealed a systematic mechanical breakdown of the WS$_2$ layers by employing doses exceeding 30 mC/cm^2, limiting the possibility to further shift the PL energy in our multigrain sample.

Strain engineering experiments that used MAMs on suspended graphene clearly showed that the induced strain in the 2D layer relaxes as a function of time due to the viscoelastic relaxation phenomena in the MAMs.[45] In order to investigate this aspect, we monitored the time evolution of the PL signal coming from the cross section of the device during an hour. The scan lines at different times reported in Fig. 3(c) show that we consistently observe a similar relaxation also in the current experiment. In Fig. 3(d), a plot of the PL energy averaged on the three central pixels as a function of time shows that the decay of the PL strain-induced redshift nicely follows an exponential law (blue dashed line) with a characteristic time of about 25 min, in agreement with what expected for a viscoelastic relaxation behavior. Moreover, we note that after the MAM actuation, the PL position does not recover its original value [green line in Fig. 3(d)], and, in addition, the subsequent PL blueshift mainly involves regions where a larger stress intensity is expected. Indeed, by considering the relative shift between the first scan line measurement after the MAM actuation ("A") and the last one ("F"), the PL blueshift largely occurs only in the

central region of the device [see Fig. 3(e)]. All these facts not only further confirm the origin of the observed shift but also indicate the possibility to use MAMs to continuously tune the strain in a wide range of intensity.

In order to have a rough but independent estimation on the deformation induced in the WS$_2$ layer, we performed numerical simulations using COMSOL Multiphysics. As described in the supplementary material, we modeled a whole device emulating the main characteristics of real devises (mechanical properties, dimensions, clamping conditions, and frictional properties). In addition, we simulated the MAM actuation by adding an initial negative and isotropic prestrain in the MAMs domains, and eventually, we let the system relax to its mechanical equilibrium. By considering a dose of 15 mC/cm^2 and our shrinkage-per-dose calibration (obtained testing devices containing discontinuous WS$_2$), numerical results indicate a volumetric component of the strain of about $\varepsilon_{xx} + \varepsilon_{yy} = 0.54\%$ at the central point of the device. As a consequence, our PL shift rate estimation is about −74 meV/%strain, with an uncertainty of about 40% mainly due to the shrinkage calibration. This gauge value is in good agreement with theoretical predictions[15,17,24] and with two out of the three available experimental works[15,16] reporting similar experiments, while it results significantly larger if compared to the remaining one.[14] The latter discrepancy might be due to a subtle but significant nonideal strain transfer efficiency that can exist in experiments that use deformable substrates.[12,16,28]

In conclusion, we studied the PL properties of a monolayer WS$_2$ stacked on top of BLG and subject to a strongly localized uniaxial tensile stress. We created such a stress configuration by combining micrometric artificial muscles with the ability of WS$_2$ to slide on graphene. The local PL energy is directly connected to the local WS$_2$ energy bandgap that we pattern with micrometric resolution by means of the induced strain profile. We obtained a maximum PL redshift of about 40 meV at the position where the top strain is expected. After the preparation of the initial MAM-induced PL redshift profile, we observed a partial and gradual tuning of the initial PL energy as a function of time, as previously reported in similar strain engineering experiments using PMMA-based MAMs. The used patternable polymeric actuators can be designed with great freedom and implemented by conventional e-beam lithography accessing a great variety of strain fields. In addition, in the present work, we demonstrated an implementation of MAMs, which does not require the creation of fragile suspended microstructures nor the transfer of WS$_2$ from its growth substrate. The combination of MAM technology with the small frictional force occurring between 2D materials bound by van der Waals interactions opens the route to advanced strain-engineered devices.

See the supplementary material for additional information concerning sliding and adhesion properties of the WS$_2$ layer, the growth of the sample, and the numerical simulation of devices.

REFERENCES

[1] K. S. Novoselov, A. Mishchenko, A. Carvalho, and A. H. Castro Neto, Science **353**, aac9439 (2016).

[2] K. S. Novoselov, D. Jiang, F. Schedin, T. J. Booth, V. V. Khotkevich, S. V. Morozov, and A. K. Geim, Proc. Natl. Acad. Sci. U. S. A. **102**, 10451 (2005).

[3] W. Choi, N. Choudhary, G. H. Han, J. Park, D. Akinwande, and Y. H. Lee, Mater. Today **20**, 116 (2017).

[4] S. Manzeli, D. Ovchinnikov, D. Pasquier, O. V. Yazyev, and A. Kis, Nat. Rev. Mater. **2**, 17033 (2017).

[5] Z. Wang, Q. Jingjing, X. Wang, Z. Zhang, Y. Chen, X. Huang, and W. Huang, Chem. Soc. Rev. **47**, 6128 (2018).

[6] F. Withers, O. Del Pozo-Zamudio, A. Mishchenko, A. P. Rooney, A. Gholinia, K. Watanabe, T. Taniguchi, S. J. Haigh, A. K. Geim, A. I. Tartakovskii, and K. S. Novoselov, Nat. Mater. **14**, 301 (2015).

[7] J. He, N. Kumar, M. Z. Bellus, H.-Y. Chiu, D. He, Y. Wang, and H. Zhao, Nat. Commun. **5**, 5622 (2014).

[8] A. Rossi, D. Spirito, F. Bianco, S. Forti, F. Fabbri, H. Büch, A. Tredicucci, R. Krahne, and C. Coletti, Nanoscale **10**, 4332 (2018).

[9] J. N. Coleman, M. Lotya, A. O'Neill, S. D. Bergin, P. J. King, U. Khan, K. Young, A. Gaucher, S. De, R. J. Smith, I. V. Shvets, S. K. Arora, G. Stanton, H.-Y. Kim, K. Lee, G. T. Kim, G. S. Duesberg, T. Hallam, J. J. Boland, J. J. Wang, J. F. Donegan, J. C. Grunlan, G. Moriarty, A. Shmeliov, R. J. Nicholls, J. M. Perkins, E. M. Grieveson, K. Theuwissen, D. W. McComb, P. D. Nellist, and V. Nicolosi, Science **331**, 568 (2011).

[10] H. R. Gutiérrez, N. Perea-López, A. L. Elías, A. Berkdemir, B. Wang, R. Lv, F. López-Urías, V. H. Crespi, H. Terrones, and M. Terrones, Nano Lett. **13**, 3447 (2013).

[11] A. Chernikov, T. C. Berkelbach, H. M. Hill, A. Rigosi, Y. Li, O. B. Aslan, D. R. Reichman, M. S. Hybertsen, and T. F. Heinz, Phys. Rev. Lett. **113**, 76802 (2014).

[12] Q. Zhang, Z. Chang, G. Xu, Z. Wang, Y. Zhang, Z.-Q. Xu, S. Chen, Q. Bao, J. Z. Liu, Y.-W. Mai, W. Duan, M. S. Fuhrer, and C. Zheng, Adv. Funct. Mater. **26**, 8707 (2016).

[13] T. Shen, A. V. Penumatcha, and J. Appenzeller, ACS Nano **10**, 4712 (2016).

[14] Y. Wang, C. Cong, W. Yang, J. Shang, N. Peimyoo, Y. Chen, J. Kang, J. Wang, W. Huang, and T. Yu, Nano Res. **8**, 2562 (2015).

[15] X. He, H. Li, Z. Zhu, Z. Dai, Y. Yang, P. Yang, Q. Zhang, P. Li, U. Schwingenschlogl, and X. Zhang, Appl. Phys. Lett. **109**, 173105 (2016).

[16] R. Frisenda, M. Drüppel, R. Schmidt, S. Michaelis de Vasconcellos, D. Perez de Lara, R. Bratschitsch, M. Rohlfing, and A. Castellanos-Gomez, Npj 2D Mater. Appl. **1**, 10 (2017).

[17] S. Fang, S. Carr, M. A. Cazalilla, and E. Kaxiras, Phys. Rev. B **98**, 75106 (2018).

[18] J. Feng, X. Qian, C.-W. Huang, and J. Li, Nat. Photonics **6**, 866 (2012).

[19] H. Li, A. W. Contryman, X. Qian, S. M. Ardakani, Y. Gong, X. Wang, J. M. Weisse, C. H. Lee, J. Zhao, P. M. Ajayan, J. Li, H. C. Manoharan, and X. Zheng, Nat. Commun. **6**, 7381 (2015).

[20] A. Castellanos-Gomez, R. Roldán, E. Cappelluti, M. Buscema, F. Guinea, H. S. J. Van Der Zant, and G. A. Steele, Nano Lett. **13**, 5361 (2013).

[21] C. Martella, C. Mennucci, A. Lamperti, E. Cappelluti, F. B. de Mongeot, and A. Molle, Adv. Mater. **30**, 1705615 (2018).

[22] J. A. Silva-Guillén, E. Canadell, F. Guinea, and R. Roldán, ACS Photonics **5**, 3231 (2018).

[23] M. A. Cazalilla, H. Ochoa, and F. Guinea, Phys. Rev. Lett. **113**, 77201 (2014).

[24] S. Aas and C. Bulutay, Opt. Express **26**, 28672 (2018).

[25] K. Liu, Q. Yan, M. Chen, W. Fan, Y. Sun, J. Suh, D. Fu, S. Lee, J. Zhou, S. Tongay, J. Ji, J. B. Neaton, and J. Wu, Nano Lett. **14**, 5097 (2014).

[26] T. M. G. Mohiuddin, A. Lombardo, R. R. Nair, A. Bonetti, G. Savini, R. Jalil, N. Bonini, D. M. Basko, C. Galiotis, N. Marzari, K. S. Novoselov, A. K. Geim, and A. C. Ferrari, Phys. Rev. B: Condens. Matter Mater. Phys. **79**, 205433 (2009).

[27] Y. Y. Hui, X. Liu, W. Jie, N. Y. Chan, J. Hao, Y. Te Hsu, L. J. Li, W. Guo, and S. P. Lau, ACS Nano **7**, 7126 (2013).

[28] G. Plechinger, A. Castellanos-Gomez, M. Buscema, H. S. J. van der Zant, G. A. Steele, A. Kuc, T. Heine, C. Schüller, and T. Korn, 2D Mater. **2**, 15006 (2015).

[29] R. Roldán, A. Castellanos-Gomez, E. Cappelluti, and F. Guinea, J. Phys. Condens. Matter **27**, 313201 (2015).

[30] R. Frisenda, A. Castellanos-Gomez, D. Perez de Lara, R. Schmidt, S. Michaelis de Vasconcellos, and R. Bratschitsch, in Optical Sensing, Imaging, Photon Counting Nanostructured Devices and Applications, edited by O. Mitrofanov, C. H. Tan, M. Razeghi, and J. L. Pau Vizcaíno (SPIE, 2017), p. 22.

[31] A. M. Dadgar, D. Scullion, K. Kang, D. Esposito, E. H. Yang, I. P. Herman, M. A. Pimenta, E.-J. G. Santos, and A. N. Pasupathy, Chem. Mater. **30**, 5148 (2018).

[32] S. P. Milovanović, L. Covaci, and F. M. Peeters, J. Appl. Phys. **125**, 82534 (2019).

[33] C. Palacios-Berraquero, D. M. Kara, A. R. P. Montblanch, M. Barbone, P. Latawiec, D. Yoon, A. K. Ott, M. Loncar, A. C. Ferrari, and M. Atatüre, Nat. Commun. **8**, 15093 (2017).

[34] J. Chaste, A. Missaoui, S. Huang, H. Henck, Z. Ben Aziza, L. Ferlazzo, C. Naylor, A. Balan, A. T. C. Johnson, R. Braive, and A. Ouerghi, ACS Nano **12**, 3235 (2018).

[35] H. J. Conley, B. Wang, J. I. Ziegler, R. F. Haglund, S. T. Pantelides, and K. I. Bolotin, Nano Lett. **13**, 3626 (2013).

[36] F. F. Settembrini, F. Colangelo, A. Pitanti, V. Miseikis, C. Coletti, R. Menichetti, R. Colle, G. Grosso, A. Tredicucci, and S. Roddaro, APL Mater. **4**, 116107 (2016).

[37] Y. Shin, M. Lozada-Hidalgo, J. L. Sambricio, I. V. Grigorieva, A. K. Geim, and C. Casiraghi, Appl. Phys. Lett. **108**, 221907 (2016).

[38] H. H. Pérez Garza, E. W. Kievit, G. F. Schneider, and U. Staufer, Nano Lett. **14**, 4107 (2014).

[39] M. Goldsche, J. Sonntag, T. Khodkov, G. J. Verbiest, S. Reichardt, C. Neumann, T. Ouaj, N. von den Driesch, D. Buca, and C. Stampfer, Nano Lett. **18**, 1707 (2018).

[40] J. W. Christopher, M. Vutukuru, D. Lloyd, J. S. Bunch, B. B. Goldberg, D. J. Bishop, and A. K. Swan, J. Microelectromech. Syst. **28**, 254 (2019).

[41] F. Colangelo, P. Pingue, V. Mišeikis, C. Coletti, F. Beltram, and S. Roddaro, 2D Mater. **6**, 25005 (2019).

[42] P. San-Jose, V. Parente, F. Guinea, R. Roldán, and E. Prada, Phys. Rev. X **6**, 31046 (2016).

[43] K. Elibol, B. C. Bayer, S. Hummel, J. Kotakoski, G. Argentero, and J. C. Meyer, Sci. Rep. **6**, 28485 (2016).

[44] C. Lee, X. Wei, J. W. Kysar, and J. Hone, Science **321**, 385 (2008).

[45] F. Colangelo, A. Pitanti, V. Mišeikis, C. Coletti, P. Pingue, D. Pisignano, F. Beltram, A. Tredicucci, and S. Roddaro, 2D Mater. **5**, 45032 (2018).

[46] H. Büch, A. Rossi, S. Forti, D. Convertino, V. Tozzini, and C. Coletti, Nano Res. **11**, 5946 (2018).

[47] Y. Kobayashi, T. Taniguchi, K. Watanabe, Y. Maniwa, and Y. Miyata, Appl. Phys. Express **10**, 45201 (2017).

[48] A. Rossi, H. Büch, C. Di Rienzo, V. Miseikis, D. Convertino, A. Al-Temimy, V. Voliani, M. Gemmi, V. Piazza, and C. Coletti, 2D Mater. **3**, 31013 (2016).

[49] Z.-Q. Xu, Y. Zhang, S. Lin, C. Zheng, Y. L. Zhong, X. Xia, Z. Li, P. J. Sophia, M. S. Fuhrer, Y.-B. Cheng, and Q. Bao, ACS Nano **9**, 6178 (2015).

[50] Y. Li, X. Li, T. Yu, G. Yang, H. Chen, C. Zhang, Q. Feng, J. Ma, W. Liu, H. Xu, Y. Liu, and X. Liu, Nanotechnology **29**, 124001 (2018).